Published in final edited form as:
Nanotechnology. 2012 February 24; 23(7): 075102. doi:10.1088/0957-4484/23/7/075102.

Gold nanostars: surfactant-free synthesis, 3D modelling, and two-photon photoluminescence imaging

Hsiangkuo Yuan[1,5], **Christopher G Khoury**[1,5], **Hanjun Hwang**[1], **Christy M Wilson**[2], **Gerald A Grant**[2], and **Tuan Vo-Dinh**[1,3,4]

Tuan Vo-Dinh: tuan.vodinh@duke.edu

[1]Department of Biomedical Engineering, Duke University, Durham, NC 27708, USA

[2]Department of Surgery, Division of Neurosurgery, Duke University Medical Center, Durham, NC, USA

[3]Department of Chemistry, Duke University, Durham, NC 27708, USA

[4]Fitzpatrick Institute for Photonics, Duke University, Durham, NC 27708, USA

Abstract

Understanding the control of the optical and plasmonic properties of unique nanosystems—gold nanostars—both experimentally and theoretically permits superior design and fabrication for biomedical applications. Here, we present a new, surfactant-free synthesis method of biocompatible gold nanostars with adjustable geometry such that the plasmon band can be tuned into the near-infrared region 'tissue diagnostic window', which is most suitable for *in vivo* imaging. Theoretical modelling was performed for multiple-branched 3D nanostars and yielded absorption spectra in good agreement with experimental results. The plasmon band shift was attributed to variations in branch aspect ratio, and the plasmon band intensifies with increasing branch number, branch length, and overall star size. Nanostars showed an extremely strong two-photon photoluminescence (TPL) process. The TPL imaging of wheat-germ agglutinin (WGA) functionalized nanostars on BT549 breast cancer cells and of PEGylated nanostars circulating in the vasculature, examined through a dorsal window chamber *in vivo* in laboratory mouse studies, demonstrated that gold nanostars can serve as an efficient contrast agent for biological imaging applications.

1. Introduction

Plasmonic gold nanoparticles (AuNPs) offer great potential for bioapplication due to their biocompatibility, chemical stability, and plasmon tunability. Because their surface resonant plasmon strongly depends on size and geometry, numerous methods have been developed to fabricate various types of AuNPs [1–4]. Particularly, the plasmons of nanoshells, nanorods, nanocages, nanostars, and hollow nanospheres can be tuned to the near-infrared (NIR) region [5–10], which is advantageous for *in vivo* application due to superior tissue penetration at that spectral range [11, 12]. Uniquely shaped nanoparticles have been used as contrast agents in optical bioimaging techniques [3, 13, 14], and as photothermal transducers for cancer treatment [7, 15–18]. To date, due to the increased demand in custom-designed bioapplication, tailoring a AuNP's plasmon for a specific application remains an active area of research.

[5]These authors contributed equally.

Online supplementary data available from stacks.iop.org/Nano/23/075102/mmedia

Star-shaped AuNPs ('nanostars') have plasmon bands that are tunable into the NIR region, and the structure contains multiple sharp branches that act as 'lightning rods' to greatly enhance the local EM-field [19–24]. According to previous calculations in 2D models, the plasmon resonant wavelength correlates with the branching [9, 25, 26]. The nanostar plasmon results from hybridization of the plasmon from each branch, while the plasmon peak intensity depends on the polarization angle [25]. The branch angle and radius are the major factors that determine the plasmon shift in a simplistic two-branch model [26]. However, understanding the plasmon behaviour of realistic nanostars consisting of 8–10 branches requires a more elaborate multi-branched model that accounts for the random incident polarization. To date, such an extensive 3D modelling of nanostars has not been reported. Nonetheless, based on the two important attributes of nanostars, NIR plasmon and strong near field enhancements at the tips, their applications have been numerous in various biomedical arenas, including surface-enhanced Raman spectroscopy (SERS) [19, 20, 27–35], photodynamic therapy [36], photothermal therapy [18], photoacoustic imaging [33], biosensing [37], and magnetomotive imaging [38].

To facilitate the bioapplication of nanostars, a biocompatible surfactant-free synthesis of nanostars in aqueous media is of particular interest. Since 2003, several 'one-pot' or seed-mediated synthesis methods have been employed using mainly poly(*N*-vinylpyrrolidone) (PVP) or cetyltrimethylammonium bromide (CTAB) as surfactant [9, 10, 21–23, 25, 26, 30, 37–41]. Silver ions were also added to improve the yield and shape owing to the underpotential deposition of silver ions on certain crystal facets of gold seeds [22–24, 39, 42, 43]. The formation of multiple branches was believed to be related to the blocking of certain facets by either the surfactant or silver ions, hence the anisotropic growth on twinned nanoparticles [22, 23, 30, 44–46]. Unfortunately, the further use of nanostars has been limited by (1) the potential toxicity of CTAB, (2) induction of aggregation following multiple washes [19], and (3) the difficulty of replacing the surfactants, PVP or CTAB, during biofunctionalization [21]. A recent report using citrate/hydroquinone as reducing/surfactant agents exemplified the potential of biocompatible nanostars on SERS imaging [34]. Therefore, achieving a surfactant-free nanostar synthesis can potentially circumvent these issues and provide a significant advancement in the development of nanostars for further applications.

One potential bioapplication of nanostars is optical imaging. Lately, efficient plasmon-enhanced two-photon photoluminescence (TPL) from non-spherical gold nanoparticles (e.g. nanorods, nanoshells, nanocages, nanostars) has been used as a contrast mechanism in several reports [6, 47–53]. A quadratic dependence of TPL intensity on excitation power and a broad emission spectrum have been observed on these NIR-plasmonic nanoparticles, but have yet to be reported on nanostars. On metal nanoparticles, the resonant coupling of the plasmon band with the incident laser greatly amplifies the nanoparticles' TPL, which originates from the recombination of electron–hole pairs [54, 55]. Typically, plasmon resonance increases the two-photon action cross sections (TPACS) of NIR-absorbing nanoparticles greatly above those of organic fluorophores [52]. TPL can therefore be applied to multiphoton microscopy, offering a convenient way to visualize NIR-absorbing gold nanoparticles using NIR excitation, which is preferable for *in vivo* imaging [12]. To date, nanostar's TPACS remains unknown and their application in *in vivo* imaging has not been reported.

In this paper we demonstrate a novel, simple, surfactant-free wet-chemistry method that produces high-yield monodisperse gold nanostars. Their optical properties and plasmon tunability have been experimentally examined and compared to polarization-averaged 3D finite element method (FEM) simulation results. The TPL behaviour of nanostars and the

use of biomolecule-functionalized nanostars as strong multiphoton contrast agents for cellular and animal imaging were investigated.

2. Experimental details

2.1. Synthesis and characterization of nanostars

All chemicals were purchased from Sigma-Aldrich (St Louis, MO) and used as received unless noted otherwise. Nanostars were prepared by a seed-mediated growth method. The seed solution was prepared by adding 15 ml of 1% citrate solution to 100 ml of boiling 1 mM $HAuCl_4$ solution under vigorous stirring. After 15 min of boiling while keeping the solution volume stable, the solution was cooled and filtered by a 0.22 μm nitrocellulose membrane, and then kept at 4 °C for long-term storage. For nanostar synthesis, 100 μl of the above citrate-stabilized seed solution (12 ± 0.7 nm; A_{520}: 2.81) was added to 10 ml of 0.25 mM auric chloride ($HAuCl_4$) solution (with 10 μl of 1 M HCl) in a 20 ml glass vial at room temperature under moderate stirring (700 rpm). Quickly, 100 μl silver nitrate ($AgNO_3$) of different concentrations (0.5–3 mM; samples named S5, S10, S20, S30 according to the $AgNO_3$ final concentration) and 50 μl of ascorbic acid (AA; 100 mM) were added simultaneously. The solution was stirred for 30 s as its colour rapidly turned from light red to blue or greenish-black. Immediately afterwards, one centrifugal wash at 3000–5000 rcf for 15 min was performed in a 15 ml tube to halt the nucleation. The solution was redispersed in DI, filtered by a 0.22 μm nitrocellulose membrane, and then kept at 4 °C for long-term storage. To obtain nanostars of similar sizes and concentrations but of different geometries, we investigated multiple factors, including pH, stirring speed, and concentration ratios of $AgNO_3$, AA, $HAuCl_4$, and seed (supporting information, figures 1–5 available at stacks.iop.org/Nano/23/075102/mmedia). In general, nanostars synthesized under lower pH, moderate vortexing speed and AA/$HAuCl_4$ ratio 1.5–2, produced the most red-shifted plasmon. More $HAuCl_4$ or fewer seeds typically yields larger nanoparticle sizes. The structural features of the nanostars were characterized using transmission electronic microscopy (TEM; Fei Tecnai G^2 Twin, 200 kV) and analysed using ImageJ software (National Institute of Health). The particle hydrodynamic size distribution and concentration were determined by nanoparticle tracking analysis (NTA 2.1; build 0342) using NanoSight NS500 (Nanosight Ltd UK). Extinction spectra were obtained using a dual-beam spectrophotometer (Shimadzu UV-3600; Shimadzu corporation, Japan).

2.2. Nanostar 3D modelling

The 3D nanostar simulations were performed using the FEM based Comsol Multiphysics v3.4 software package and the RF module (Comsol, Inc. Burlington MA, USA). A unique 3D nanostar model was designed for each of the samples S5, S10, S20, and S30 using the dimensions obtained from their corresponding TEM images (supporting information, table 1 available at stacks.iop.org/Nano/23/075102/mmedia). For a particular star model, the branches protrude normal to the core surface, but were randomly positioned on the core such as to maximize the inter-branch distance. The dielectric function of gold was modelled using the Lorentz–Drude model for gold from Johnston and Christy [56], and the surrounding medium was modelled as water with a refractive index $n = 1.33$. The computational domain was bounded by a spherical perfectly matched layer (PML) to prevent any reflections back onto the nanoparticle. The nanostars were excited with a z-polarized incident plane wave of E-field amplitude 1, propagating along the y-axis and of wavelength range 300–1200 nm. The nanoparticles were meshed such that the largest mesh size on the star's surface was limited to 3 nm, ensuring high meshing density and thus good spatial sampling. The orientation dependence of the incident E-field was accounted for by averaging the absorption spectra of the nanostars as they were incrementally rotated by 30° in the [$x = y$]

plane, such that the orientation of the branches relative to the *z*-polarized incident field became randomized.

2.3. TPL characterization and in vitro/in vivo imaging of nanostars

2.3.1. Nanostars TPL characterization—The TPL images were recorded using a commercial multiphoton microscope (Olympus FV1000, Olympus America, Center Valley, PA) with three detection channels (420–460, 495–540, 575–630 nm) on photomultiplier tubes (Hamamatsu, Bridgewater, NJ). A femtosecond Ti:sapphire laser (Chameleon Vision II, Coherent, Santa Clara, CA) with tunable range 680–1080 nm, 140 fs pulse width and 80 MHz repetition rate was used. The laser beam was focused through a 25 × 1.05 NA water-immersion objective (XLPL25XWMP, Olympus America, Center Valley, PA). The TPACS of gold nanostars were measured by comparing the TPL of nanostars (0.1 nM in DI) with fluorescence of Rhodamine B (100 nM in pure MeOH) at 800 nm excitation. The TPACS has a unit of cm^4 s, where 1 Göeppert–Mayer unit (GM) represents 10^{-50} cm^4 s $photon^{-1}$. TPACS is the product of the fluorescence quantum yield (Φ) and the absolute two-photon absorption cross-section (δ) [57]. Nanostars' TPACS is determined by

$$\Phi_S \sigma_S = \frac{F_S}{F_R} \times \frac{C_R}{C_S} \times \Phi_R \sigma_R$$

where F_S and F_R are the integrated luminescence/fluorescence intensity of nanostars and Rhodamine B; C_S and C_R are the concentrations of nanostars and Rhodamine B. The excitation power was 2 mW. Luminescence/fluorescence intensity was integrated over an image area of 250 × 250 μm^2 under 10 μs/pixel at 256 × 256 resolution. The sample solution was placed on a depression slide covered by a coverslip during imaging.

2.3.2. Nanostars TPL cellular imaging—The BT549 cancer cells were a gift from Dr Victoria Seewaldt. Cells were incubated in RPMI 1640 medium (Invitrogen; Carlsbad, CA) containing 10% of foetal bovine serum (FBS), 25 mM HEPES and 0.023 U ml^{-1} of insulin, in an incubator with a humidified atmosphere (37 °C, 5% CO_2). Cells in exponential growth phase were used in experiments. Nanostars were conjugated with wheat-germ agglutinin (WGA) using a hetero-bifunctional crosslinker, OPSS-PEG_{2000}-NHS (Creative PEGworks; Winston Salem, NC), based on a previous protocol [58]. WGA has high affinity to glyco-proteins and glycolipids on the cell membrane; therefore, WGA-conjugated nanostars can label the cell membrane and be visualized on the cell surface. Nanostars conjugated with $SHPEG_{5000}$ (*O*-[2-(3-mercaptopropionylamino)ethyl]-*O*′-methylpolyethylene glycol, MW 5000) were used as a control. Functionalized nanostars were washed and resuspended to a final concentration 0.1 nM in phosphate buffer saline (PBS). The cells were fixed with paraformaldehyde (4%, 10 min), blocked with 10% FBS for 3 min and washed with PBS twice. They then underwent 10 min incubation with WGA-nanostars or PEG-nanostars followed by two PBS washes. Counterstaining with Hoescht 33342 and FM 1-43 FX was performed according to the company's protocols (Invitrogen; Carlsbad, CA). Two-photon imaging was done under 1% transmission, 10 μs/pixel and 512 × 512 resolution with four-frame Kalman averaging. All three channels were set to 550 gain (for WGA-nanostar) or 600 gain (for PEG-nanostar) and 8 offset.

2.3.3. Nanostars TPL animal imaging—Nanostar (S30) 100 ml was PEGylated and concentrated to 50 nM in PBS after two centrifugal washes. Female CD31 nu/nu mice were anaesthetized with an intra-peritoneal injection of ketamine/xylazine (10/100 mg/kg). Anaesthetized animals were then placed on a heating frame to maintain body temperature at

37 °C. Two-photon imaging was performed through a dorsal window chamber following 50 μl PEGylated gold nanostars (50 nM) injection retro-orbitally (RO). As control, another mouse was injected with 50 μl of PBS RO. All procedures were approved by the Duke University Institutional Animal Care and Use Committee.

3. Results and discussion

3.1. Surfactant-free synthesis and plasmon tunability of nanostars

We report for the first time a surfactant-free synthesis of nanostars that achieves high monodispersity and plasmon tunability, which has not been demonstrated before [34, 40, 59–62]. The synthesis is extremely simple and the reaction is completed in less than 30 s at room temperature, resulting in particles of around 60 nm diameters with narrow size distribution (figure 1 top). The reagents used are similar to previous silver-assisted seed-mediated nanostar or nanorod recipes [20–23, 30, 38, 39, 44, 63], except for the omission of any CTAB or PVP surfactants. This new synthesis was discovered by methodically tweaking a number of variables as described below. (1) The AA needs to be added fast; drop-wise addition leads to sphere formation. (2) The presence of Ag^+ is necessary for nanostar formation. Without Ag^+, it forms polydisperse rods and spheres. It is believed that the major role of Ag^+ is not to form Ag branches but to assist the anisotropic growth of Au branches on certain crystallographic facets on multi-twinned citrate seeds, but not single crystalline CTAB seeds [22, 23, 45, 46]. Silver may constitute 2–4.5% of the Au branch as in nanorods [45]. (3) Lowering the pH by addition of a small amount of HCl promotes further red-shifted plasmons (supporting information, figure 1 available at stacks.iop.org/Nano/23/075102/mmedia). Slow intra-particle smoothing at lower pH may play a role [64]. Since adding the same concentration of nitric acid did not form nanostars, the chloride ion may behave similarly to the iodide ion influencing the anisotropic growth [65]. (4) Because each AA molecule can donate two electrons, the complete reduction of Au^{3+} requires the ratio AA:$HAuCl_4$ to be higher than 3:2. Similar to Ahmed *et al*'s finding [22], a higher ratio leads to the formation of less spiky nanostars (supporting information, figure 2 available at stacks.iop.org/Nano/23/075102/mmedia). (5) Without seeds, the reaction forms nanostars of bigger size (>100 nm diameter). With more seeds, the resulting nanostars get smaller (supporting information, figure 3 available at stacks.iop.org/Nano/23/075102/mmedia). (6) The $Ag^+$and AA need to be added together. If Ag^+ is added too early, the silver chloride precipitates and no nanostars are formed when AA is added. If Ag^+ is added too late, larger gold spheres have already formed from the addition of AA. With all these variables carefully controlled, a successful and repeatable recipe for surfactant-free synthesis of nanostars was developed. The major advantage of this recipe is the simplicity and absence of surfactant; the nanostars are biocompatible and can be conjugated easily with biomolecules for further applications.

Plasmon tunability was achieved by adjusting the Ag^+ concentration using a constant seed amount in our study. Previously, plasmon tunability was achieved by adjusting the ratio of auric chloride to seed hence forming nanostars of different sizes [10]. In our study, similar to the growth of nanorods [63], adding higher concentrations of Ag^+ progressively red-shifted the plasmon band by forming longer, sharper, and more numerous branches with small overall size variation (figure 1). S5 consists of a few protrusions, while S30 comprises multiple long, sharp branches that appear to branch even further. The nanostars' plasmon peaks are tunable from 600 to 1000 nm by adjusting the Ag^+ concentration (figure 2(a)). This is accompanied by a visible change in the solution colour from dark blue to dark grey as the plasmon red-shifts and broadens. Both the plasmon peak position and spectral width followed a linear trend with increasing Ag^+ concentration. A plateau was reached around an Ag^+ concentration of 30 μM in this recipe (supporting information, figure 5 available at stacks.iop.org/Nano/23/075102/mmedia). Nanostars can therefore be synthesized in a

controlled fashion and exploited as potential candidates for NIR excitation and absorption in the 'diagnostic window' for biomedical applications.

3.2. Polarization-averaged 3D nanostar modelling

This paper models and compares the optical properties of different nanostars (S5–S30). Instead of modelling the plasmon of a single polarization, our analysis features polarization-averaging over space as the nanostars were discretely rotated at six angles, a feature that has not been addressed so far. The 3D nanostar simulations were performed using the FEM, which yields solutions to the local E-field around 3D metallic nanostructures that are in excellent agreement with the theory [66, 67].

Figure 1 depicts that for each of the four nanostars, the local E-field is most greatly enhanced at the tips of those branches that are aligned at least partially parallel to the incident polarization. The enhancement was greatest when the particle's plasmon matches the incident energy. S20, which plasmon peak matches the 800 nm laser line, and has the strongest field enhancement among other nanostars. Also, the E-field along the surface of the branch is enhanced to a value of at least between 1 and 4, suggesting that these surfaces also contribute to the total E-field enhancement around the nanostar.

We demonstrate that the experimental absorption peak shifts can be properly modelled using a 3D nanostar geometry designed according to the parameters in supporting information table 1 (available at stacks.iop.org/Nano/23/075102/mmedia), namely, core diameter, branch base width, branch length, and tip radius. The modelled absorption peaks of the various nanostars align well with the experimentally measured spectra, and reproduce experimentally observed peaks for each nanostar solution sample (figure 2(b)). Similar to previous findings that the plasmon of a nanostar results from hybridization of plasmons of the core and the branches [59], the plasmon spectrum in our study shows a weak absorption around 520 nm attributed to the plasmon resonance of the nanostar's core, and a dominant plasmon band at longer wavelengths due to the resonance supported by the nanostar branches. As the number of branches increases from 4 to 10 for S5 to S30, respectively, the plasmon red-shifts, peak absorption cross-section increases, and the SD of the averaged spectrum data points decrease.

Our study showed that the plasmon shift is controlled mainly by the branch aspect ratio (AR): branch length divided by base width. Figure 2(c) shows the progression of absorption peak position and intensity along with AR. A linear relationship was demonstrated between the absorption peak position and AR, either by adjusting branch length while keeping branch width constant (figure 2(c)) or vice versa (supporting information, figure 6 available at stacks.iop.org/Nano/23/075102/mmedia). Tip angle, however, does not correlate as linearly as AR to the peak position (supporting information, figure 6 available at stacks.iop.org/Nano/23/075102/mmedia). Branches with varying tip radius or angle but the same aspect ratio result in the same peak position (supporting information, figure 7 available at stacks.iop.org/Nano/23/075102/mmedia). Consistent with Hao *et al*'s finding, the polarization only affects the peak intensity but not the peak position (supporting information, figure 8 available at stacks.iop.org/Nano/23/075102/mmedia) [25]. Also, we found that the peak intensity increases with increasing branch number, branch length, and core size (figure 2(c); supporting information, figures 9 and 10 available at stacks.iop.org/Nano/23/075102/mmedia). It is noteworthy that the core size only contributes to the 520 nm peak, whereas the branch geometry determines the plasmon position and intensity in the NIR. Meanwhile, the geometrical parameters that do not significantly affect the plasmon shift include nanostar core size, branch length (assuming constant AR), and branch number beyond at least two oppositely positioned branches (supporting information, figures 9–11 available at stacks.iop.org/Nano/23/075102/mmedia).

It is clear, however, that the calculated plasmon resonance widths are significantly narrower than the experimental data. This experimental broadening is likely due to the nonuniform nanostar geometries (e.g. wide distribution of AR), as well as the finite-size effects, which broaden and dampen the resonance but do not influence the plasmon band position [66, 68].

3.3. Nanostars TPL characterization and imaging

3.3.1. Nanostar TPL characterization—Gold nanostars, with plasmons in the NIR, show greatly enhanced TPL. A quadratic dependence of TPL intensity on excitation power (below 10 mW) suggests the existence of an underlying nonlinear two-photon upconverting process on nanostars (figure 3(a)). Such dependence was not seen on 60 nm gold or silver nanospheres solution when examined by the same system (data not shown). However, at higher excitation power, the dependence became close to linear (supporting information, figure 12 available at stacks.iop.org/Nano/23/075102/mmedia), which may be a consequence of the increasing competition between linear decay and upconversion for the depletion of the intermediate excited states [69]. Figure 3(b) shows that the TPL excitation spectra of S20 and S30 match their plasmon spectra, indicating that nanostars enhance TPL via plasmon coupling [51]. Interestingly, the concentration normalized emission intensity at 800 nm of nanostars solutions were found to be 1.1×10^4 greater than that of Rhodamine B, making the TPACS of nanostars more than a million GM units. This value is significantly higher than TPACS of quantum dots [57]. Meanwhile, the emission intensities from each nanostar solution were found to be similar on three different detection channels on the microscope, hence appearing as a white colour on imaging. The broad emission spectrum implies that TPL from nanostars may originate from electron–hole recombination as has been observed on nanorods [51, 55, 70]. The exact mechanism of TPL from nanostars will be further investigated in future studies.

3.3.2. Nanostar TPL cellular imaging—Polymer-free nanostars with such a high TPACS can be used as a strong contrast agent in TPL imaging in biological samples. Here we demonstrate TPL imaging of wheat-germ agglutinin (WGA) functionalized nanostars (S30) on paraformaldehyde-fixed BT549 cancer cells. Figure 4(a) shows a preferential binding of WGA-coated nanostars on the cell membrane. In contrast, PEG-coated nanostars bound poorly (figure 4(b)). Numerous white spots representing nanostars covered the cell membrane in preference to the cytoplasm. The observed white colour was a composite result of the similar intensity on three different detection channels, indicating a broad TPL emission spectrum from nanostars. The nanostars emitted strongly without photobleaching under low laser power (4 mW), which is in the typical working range for organic fluorophores. In contrast, a signal from WGA-coated spheres can only be observed under much stronger excitation power (data not shown).

3.3.3. Nanostar TPL animal imaging—Previously, tracking gold nanoparticles *in vivo* remained a difficult task optically. Under fluorescence microscopy, organic fluorophores insufficiently light up AuNPs due to quenching, requiring manipulation of the distance between the fluorophore and the metal surface [71]. Dark field microscopy and differential interference contrast microscopy can both visualize AuNPs in cells but are not available for tissue. Exploiting its strong TPACS feature, nanostar imaging and tracking without the need for fluorophores is possible. We demonstrated the TPL imaging of PEGylated nanostars through a dorsal window chamber on nude mice. Within 5 min after injection, PEGylated nanostars travelled along the blood vessel where the tissue vasculature became clearly visible at rather low excitation power (1–5% transmission) with minimal tissue autofluorescence background (figure 4(c)). PEGylation acts as a protective barrier on the nanostars to prevent them from aggregation in physiological conditions and to extend their serum half-life from immunoclearance [72]. Because of the high TPACS of nanostars,

tracking the motion of PEGylated nanostars in the blood vessel can be obtained as well (supporting information, movie 1 available at stacks.iop.org/Nano/23/075102/mmedia). Without nanostars or dyes, the excitation power needed to be greatly increased (20% transmission) before seeing the autofluorescence from blood vessels and tissue (figure 4(d)). Clearly, gold nanostars act as strong contrast agents under TPL microscopy. Throughout the study period, no apparent toxicity from PEGylated nanostars was observed. The ability of using optical microscopy to visualize metal nanoparticles greatly simplifies tracking and possibly quantifying gold nanostars for both *in vitro* and *in vivo* applications.

4. Conclusion

We have synthesized surfactant-less, plasmon tunable gold nanostars that enable simple surface functionalization. The synthesis is quick and polymer-free. As branch AR increases from nanostar samples S5 to S30, the plasmon peaks shift to the NIR region. Sharp branches interact more intensely with NIR laser excitation, and play a key role in determining the optical properties of the nanostars. Three-dimensional models of the nanostars were numerically solved to exhibit a good agreement between experimental and theoretical absorption spectra, with the branch length and number contributing to peak intensity, and branch AR to the plasmon shift. In addition, because the nanostar's plasmon matches the NIR laser excitation, a TPACS of one million GM was found. Exploiting the high TPACS, we showed for the first time that nanostars can be used as a strong contrast agent for two-photon photoluminescence microscopy for both *in vitro* and *in vivo* studies. Combining the high NIR absorption, high TPACS, and simple fabrication, polymer-free gold nanostars have great potential in biomedical imaging and diagnostic applications.

Supplementary Material

Refer to Web version on PubMed Central for supplementary material.

Acknowledgments

The authors would like to thank Dr Sam Johnson for his expertise on multiphoton microscopy and Dr Guy Griffin for his professional comments. This work was sponsored by the National Institutes of Health (Grants R01 EB006201 and R01 ES014774) and the Department of Defence (W81XWH-09-1-0064).

References

1. Lal S, Link S, Halas NJ. Nano-optics from sensing to waveguiding. Nature Photon. 2007; 1:641–8.
2. Vo-Dinh T, Dhawan A, Norton SJ, Khoury CG, Wang H-N, Misra V, Gerhold MD. Plasmonic nanoparticles and nanowires: design, fabrication and application in sensing. J Phys Chem C. 2010; 114:7480–8.
3. Sau TK, Rogach AL, Jäckel F, Klar TA, Feldmann J. Properties and applications of colloidal nonspherical noble metal nanoparticles. Adv Mater. 2010; 22:1805–25. [PubMed: 20512954]
4. Burda C, Chen X, Narayanan R, El-Sayed M. Chemistry and properties of nanocrystals of different shapes. Chem Rev. 2005; 105:1025–102. [PubMed: 15826010]
5. Huang X, Neretina S, El-Sayed MA. Gold nanorods: from synthesis and properties to biological and biomedical applications. Adv Mater. 2009; 21:4880–910.
6. Xia Y, Li W, Cobley CM, Chen J, Xia X, Zhang Q, Yang M, Cho EC, Brown PK. Gold nanocages: from synthesis to theranostic applications. Acc Chem Res. 2011; 44:914–24. [PubMed: 21528889]
7. Zhang J. Biomedical applications of shape-controlled plasmonic nanostructures: a case study of hollow gold nanospheres for photothermal ablation therapy of cancer. J Phys Chem Lett. 2010; 1:686–95.

8. Atkinson RL, Zhang M, Diagaradjane P, Peddibhotla S, Contreras A, Hilsenbeck SG, Woodward WA, Krishnan S, Chang JC, Rosen JM. Thermal enhancement with optically activated gold nanoshells sensitizes breast cancer stem cells to radiation therapy. Sci Transl Med. 2010; 2:55ra79.
9. Trigari S, Rindi A, Margheri G, Sottini S, Dellepiane G, Giorgetti E. Synthesis and modelling of gold nanostars with tunable morphology and extinction spectrum. J Mater Chem. 2011; 21:6531–40.
10. Barbosa S, Agrawal A, Rodriguez-Lorenzo L, Pastoriza-Santos I, Alvarez-Puebla RA, Kornowski A, Weller H, Liz-Marzan LM. Tuning size and sensing properties in colloidal gold nanostars. Langmuir. 2010; 26:14943–50. [PubMed: 20804155]
11. Hahn MA, Singh AK, Sharma P, Brown SC, Moudgil BM. Nanoparticles as contrast agents for *in vivo* bioimaging: current status and future perspectives. Anal Bioanal Chem. 2011; 399:3–27. [PubMed: 20924568]
12. Weissleder R. A clearer vision for *in vivo* imaging. Nature Biotechnol. 2001; 19:316–7. [PubMed: 11283581]
13. Boisselier E, Astruc D. Gold nanoparticles in nanomedicine: preparations, imaging, diagnostics, therapies and toxicity. Chem Soc Rev. 2009; 38:1759–82. [PubMed: 19587967]
14. Sperling RA, Rivera Gil P, Zhang F, Zanella M, Parak WJ. Biological applications of gold nanoparticles. Chem Soc Rev. 2008; 37:1896–908. [PubMed: 18762838]
15. Huang X, El-Sayed M. Gold nanoparticles: optical properties and implementations in cancer diagnosis and photothermal therapy. J Adv Res. 2010; 1:13–28.
16. Chen J, Glaus C, Laforest R, Zhang Q, Yang M, Gidding M, Welch MJ, Xia Y. Gold nanocages as photothermal transducers for cancer treatment. Small. 2010; 6:811–7. [PubMed: 20225187]
17. Lal S, Clare S, Halas NJ. Nanoshell-enabled photothermal cancer therapy: impending clinical impact. Acc Chem Res. 2008; 41:1842–51. [PubMed: 19053240]
18. Van de Broek B, Devoogdt N, D'Hollander A, Gijs H-L, Jans K, Lagae L, Muyldermans S, Maes G, Borghs G. Specific cell targeting with nanobody conjugated branched gold nanoparticles for photothermal therapy. ACS Nano. 2011; 5:4319–28. [PubMed: 21609027]
19. Rodriguez-Lorenzo L, Alvarez-Puebla RA, Javier Garcia de Abajo F, Liz-Marzán LM. Surface enhanced raman scattering using star-shaped gold colloidal nanoparticles. J Phys Chem C. 2010; 114:7336–40.
20. Nalbant Esenturk E, Hight Walker A. Surface-enhanced Raman scattering spectroscopy via gold nanostars. J Raman Spectrosc. 2009; 40:86–91.
21. Khoury C, Vo-Dinh T. Gold nanostars for surface-enhanced raman scattering: synthesis, characterization and optimization. J Phys Chem C. 2008; 112:18849–59.
22. Ahmed W, Kooij ES, van Silfhout A, Poelsema B. Controlling the morphology of multi-branched gold nanoparticles. Nanotechnology. 2010; 21:125605. [PubMed: 20203353]
23. Kawamura G, Yang Y, Fukuda K, Nogami M. Shape control synthesis of multi-branched gold nanoparticles. Mater Chem Phys. 2009; 115:229–34.
24. Nehl C, Liao H, Hafner J. Optical properties of star-shaped gold nanoparticles. Nano Lett. 2006; 6:683–8. [PubMed: 16608264]
25. Hao F, Nehl CL, Hafner JH, Nordlander P. Plasmon resonances of a gold nanostar. Nano Lett. 2007; 7:729–32. [PubMed: 17279802]
26. Kumar P, Pastoriza-Santos I, Rodríguez-González B, Abajo F, Liz-Marzán L. High-yield synthesis and optical response of gold nanostars. Nanotechnology. 2008; 19:015606. [PubMed: 21730541]
27. Hrelescu C, Sau TK, Rogach AL, Jackel F, Feldmann J. Single gold nanostars enhance Raman scattering. Appl Phys Lett. 2009; 94:153113.
28. Abalde-Cela S, Aldeanueva-Potel P, Mateo-Mateo C, Rodríguez-Lorenzo L, Alvarez-Puebla RA, Liz-Marzán LM. Surface-enhanced Raman scattering biomedical applications of plasmonic colloidal particles. J R Soc Interface. 2010; 7(Suppl 4):S435–50. [PubMed: 20462878]
29. Rodriguez-Lorenzo L, Alvarez-Puebla RA, Pastoriza-Santos I, Mazzucco S, Stephan O, Kociak M, Liz-Marzán LM, Garcia de Abajo FJ. Zeptomol detection through controlled ultrasensitive surface-enhanced Raman scattering. J Am Chem Soc. 2009; 131:4616–8. [PubMed: 19292448]

30. Guerrero-Martínez A, Barbosa S, Pastoriza-Santos I, Liz-Marzán LM. Nanostars shine bright for you. Curr Opin Colloid Interface Sci. 2011; 16:118–27.
31. Lu W, Singh AK, Khan SA, Senapati D, Yu H, Ray PC. Gold nano-popcorn-based targeted diagnosis, nanotherapy treatment, and *in situ* monitoring of photothermal therapy response of prostate cancer cells using surface-enhanced Raman spectroscopy. J Am Chem Soc. 2010; 132:18103–14. [PubMed: 21128627]
32. Su Q, Ma X, Dong J, Jiang C, Qian W. A reproducible SERS substrate based on electrostatically assisted APTES-functionalized surface-assembly of gold nanostars. ACS Appl Mater Interfaces. 2011; 3:1873–9. [PubMed: 21528839]
33. Kim C, Song H-M, Cai X, Yao J, Wei A, Wang LV. *In vivo* photoacoustic mapping of lymphatic systems with plasmon-resonant nanostars. J Mater Chem. 2011; 21:2841–4. [PubMed: 21660122]
34. Schütz M, Steinigeweg D, Salehi M, Kömpe K, Schlücker S. Hydrophilically stabilized gold nanostars as SERS labels for tissue imaging of the tumor suppressor p63 by immuno-SERS microscopy. Chem Commun. 2011; 47:4216–8.
35. Rodriguez-Lorenzo L, Krpetic Z, Barbosa S, Alvarez-Puebla RA, Liz-Marzán LM, Prior IA, Brust M. Intracellular mapping with SERS-encoded gold nanostars. Integr Biol. 2011; 3:922–6.
36. Fales AM, Yuan H, Vo-Dinh T. Silica-coated gold nanostars for combined surface-enhanced Raman scattering (SERS) detection and singlet-oxygen generation: a potential nanoplatform for theranostics. Langmuir. 2011; 27:12186–90. [PubMed: 21859159]
37. Dondapati SK, Sau TK, Hrelescu C, Klar TA, Stefani FD, Feldmann J. Label-free biosensing based on single gold nanostars as plasmonic transducers. ACS Nano. 2010; 4:6318–22. [PubMed: 20942444]
38. Song H-M, Wei Q, Ong QK, Wei A. Plasmon-resonant nanoparticles and nanostars with magnetic cores: synthesis and magnetomotive imaging. ACS Nano. 2010; 4:5163–73. [PubMed: 20690598]
39. Wu H-L, Chen C-H, Huang MH. Seed-mediated synthesis of branched gold nanocrystals derived from the side growth of pentagonal bipyramids and the formation of gold nanostars. Chem Mater. 2009; 21:110–4.
40. Zou X, Ying E, Dong S. Seed-mediated synthesis of branched gold nanoparticles with the assistance of citrate and their surface-enhanced Raman scattering properties. Nanotechnology. 2006; 17:4758–64. [PubMed: 21727609]
41. Chen S, Wang ZL, Ballato J, Foulger SH, Carroll DL. Monopod, bipod, tripod, and tetrapod gold nanocrystals. J Am Chem Soc. 2003; 125:16186–7. [PubMed: 14692749]
42. Chen H, Kou X, Yang Z, Ni W, Wang J. Shape-and size-dependent refractive index sensitivity of gold nanoparticles. Langmuir. 2008; 24:5233–7. [PubMed: 18435552]
43. Sau TK, Murphy CJ. Room temperature, high-yield synthesis of multiple shapes of gold nanoparticles in aqueous solution. J Am Chem Soc. 2004; 126:8648–9. [PubMed: 15250706]
44. Sau TK, Rogach AL, Döblinger M, Feldmann J. One-step high-yield aqueous synthesis of size-tunable multispiked gold nanoparticles. Small. 2011; 7:2188–94. [PubMed: 21630442]
45. Orendorff C, Murphy C. Quantitation of metal content in the silver-assisted growth of gold nanorods. J Phys Chem B. 2006; 110:3990–4. [PubMed: 16509687]
46. Liu M, Guyot-Sionnest P. Mechanism of silver(I)-assisted growth of gold nanorods and bipyramids. J Phys Chem B. 2005; 109:22192–200. [PubMed: 16853888]
47. Durr NJ, Larson T, Smith DK, Korgel BA, Sokolov K, Ben-Yakar A. Two-photon luminescence imaging of cancer cells using molecularly targeted gold nanorods. Nano Lett. 2007; 7:941–5. [PubMed: 17335272]
48. Bickford L, Sun J, Fu K, Lewinski N. Enhanced multi-spectral imaging of live breast cancer cells using immunotargeted gold nanoshells and two-photon excitation microscopy. Nanotechnology. 2008; 19:315102. [PubMed: 21828779]
49. Kumar S, Harrison N, Richards-Kortum R, Sokolov K. Plasmonic nanosensors for imaging intracellular biomarkers in live cells. Nano Lett. 2007; 7:1343–38.
50. Martinez Maestro L, Martin Rodriguez E, Vetrone F, Naccache R, Loro Ramirez H, Jaque D, Capobianco JA, Garcia Sole J. Nanoparticles for highly efficient multiphoton fluorescence bioimaging. Opt Express. 2010; 18:23544–53. [PubMed: 21164698]

51. Tong L, Wei Q, Wei A, Cheng J-X. Gold nanorods as contrast agents for biological imaging: optical properties, surface conjugation and photothermal effects. Photochem Photobiol. 2009; 85:21–32. [PubMed: 19161395]
52. Wang H, Huff TB, Zweifel DA, He W, Low PS, Wei A, Cheng J-X. *In vitro* and *in vivo* two-photon luminescence imaging of single gold nanorods. Proc Natl Acad Sci USA. 2005; 102:15752–6. [PubMed: 16239346]
53. Wei Q, Wei A. Optical imaging with dynamic contrast agents. Chem Eur J. 2011; 17:1080–91. [PubMed: 21243670]
54. Dulkeith E, Niedereichholz T, Klar T, Feldmann J, von Plessen G, Gittins D, Mayya K, Caruso F. Plasmon emission in photoexcited gold nanoparticles. Phys Rev B. 2004; 70:205424.
55. Link S, El-Sayed MA. Optical properties and ultrafast dynamics of metallic nanocrystals. Annu Rev Phys Chem. 2003; 54:331–66. [PubMed: 12626731]
56. Johnson PB, Christy RW. Optical constants of the noble metals. Phys Rev B. 1972; 6:4370–9.
57. Zipfel WR, Williams RM, Webb WW. Nonlinear magic: multiphoton microscopy in the biosciences. Nature Biotechnol. 2003; 21:1369–77. [PubMed: 14595365]
58. Hirsch LR, Halas NJ, West JL. Whole-blood immunoassay facilitated by gold nanoshell-conjugate antibodies. Methods Mol Biol. 2005; 303:101–11. [PubMed: 15923678]
59. Hao E, Bailey R, Schatz G, Hupp J, Li S. Synthesis and optical properties of 'branched' gold nanocrystals. Nano Lett. 2004; 4:327–30.
60. Wang Z, Zhang J, Ekman JM, Kenis PJA, Lu Y. DNA-mediated control of metal nanoparticle shape: one-pot synthesis and cellular uptake of highly stable and functional gold nanoflowers. Nano Lett. 2010; 10:1886–91. [PubMed: 20405820]
61. Xie J, Lee JY, Wang DIC. Seedless, surfactantless, high-yield synthesis of branched gold nanocrystals in HEPES buffer solution. Chem Mater. 2007; 19:2823–30.
62. Bakr O, Wunsch B, Stellacci F. High-yield synthesis of multi-branched urchin-like gold nanoparticles. Chem Mater. 2006; 18:3297–301.
63. Nikoobakht B, El-Sayed M. Preparation and growth mechanism of gold nanorods (NRs) using seed-mediated growth method. Chem Mater. 2003; 15:1957–62.
64. Ji X, Song X, Li J, Bai Y, Yang W, Peng X. Size control of gold nanocrystals in citrate reduction: the third role of citrate. J Am Chem Soc. 2007; 129:13939–48. [PubMed: 17948996]
65. Grzelczak M, Sanchez-Iglesias A, Rodríguez-Gonzalez B, Alvarez-Puebla R, Perez-Juste J, Liz-Marzán LM. Influence of iodide ions on the growth of gold nanorods: tuning tip curvature and surface plasmon resonance. Adv Funct Mater. 2008; 18:3780–6.
66. Khoury CG, Norton SJ, Vo-Dinh T. Investigating the plasmonics of a dipole-excited silver nanoshell: Mie theory versus finite element method. Nanotechnology. 2010; 21:315203. [PubMed: 20634565]
67. Khoury CG, Norton SJ, Vo-Dinh T. Plasmonics of 3D nanoshell dimers using multipole expansion and finite element method. ACS Nano. 2009; 3:2776–88. [PubMed: 19678677]
68. Prodan E, Nordlander P, Halas NJ. Electronic structure and optical properties of gold nanoshells. Nano Lett. 2003; 3:1411–5.
69. Pollnau M, Gamelin D, Lüthi S, Güdel H, Hehlen M. Power dependence of upconversion luminescence in lanthanide and transition-metal-ion systems. Phys Rev B. 2000; 61:3337–46.
70. Wang D-S, Hsu F-Y, Lin C-W. Surface plasmon effects on two photon luminescence of gold nanorods. Opt Express. 2009; 17:11350–9. [PubMed: 19582049]
71. Jang B, Park J-Y, Tung C-H, Kim I-H, Choi Y. Gold nanorod-photosensitizer complex for near-infrared fluorescence imaging and photodynamic/photothermal therapy *in vivo*. ACS Nano. 2011; 5:1086–94. [PubMed: 21244012]
72. Huang X, Peng X, Wang Y, Wang Y, Shin DM, El-Sayed MA, Nie S. A reexamination of active and passive tumor targeting by using rod-shaped gold nanocrystals and covalently conjugated peptide ligands. ACS Nano. 2010; 4:5887–96. [PubMed: 20863096]

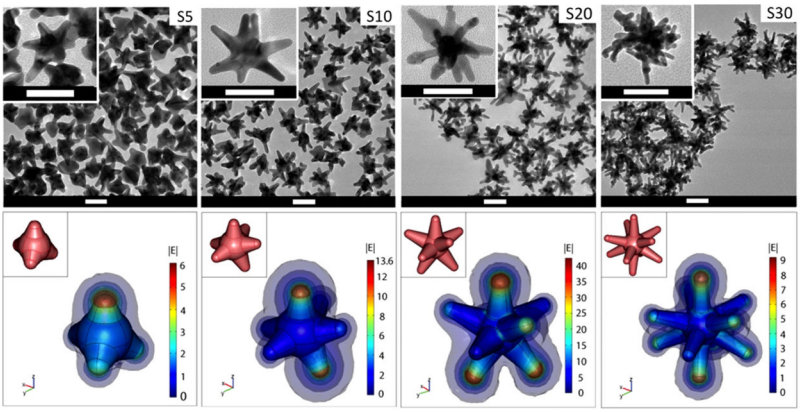

Figure 1.

(Top) TEM images of nanostars formed under different Ag^+ concentrations (S5: 5 μM, S10: 10 μM, S20: 20 μM, S30: 30 μM). The scale bar is 50 nm. (Bottom) Simulation of $|E|$ in the vicinity of the nanostars in response to a *z*-polarized plane wave incident E-field of unit amplitude, propagating in the *y*-direction, and with a wavelength of 800 nm. E-field enhancement is greatest on S20. The insets depict the 3D geometry of the stars. Diagrams are not to scale.

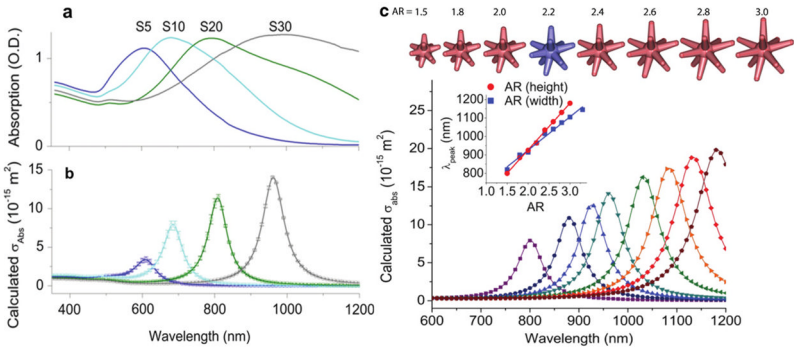

Figure 2.

(a) Extinction spectra of the star solutions (~0.1 nM) in DI. (b) The corresponding calculated absorption spectra of nanostars embedded in water. The data points (±1 SD) were interpolated with a spline fit. (c) The scatter plots of polarization-averaged absorption against aspect ratio (AR) tuned by varying branch height while keeping the base width, core and tip diameters, and branch number, constant. Their corresponding 3D geometry is on top, where the blue one is the original model for S30 nanostars. (Inset) The linear relationship between the plasmon peak position and AR, which is tuned by varying branch height (red, $R^2 = 0.997$) or base width (blue, $R^2 = 0.987$) while keeping all other parameters constant.

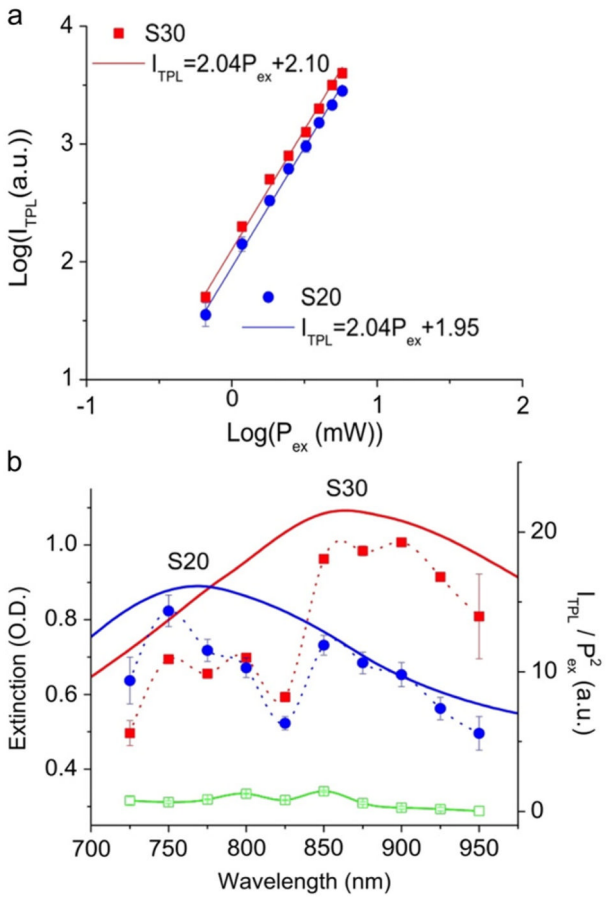

Figure 3.

(a) The quadratic dependence of the I_{TPL} to the P_{ex} from S20 and S30 solution (0.1 nM). The laser was set at 800 nm with power adjusted between 0.5 and 6 mW. Scatter plots (±1 SD) were displayed with linearly fitted lines. (b) Plasmon spectra (solid lines) and TPL excitation spectra (spline-fitted dashed lines ±1 SD) of S20 (blue) and S30 (red) nanostars 0.1 nM in citrate buffer, and Rhodamine B (green) 100 nM in MeOH. The emission intensity (I_{TPL}) spectra were normalized by the excitation power square ($P_{ex}{}^2$). The excitation power was kept under 2 mW throughout the measurement. Signal intensities were integrated over 250 × 250 μm^2. The spectral dip at 825 nm seen on both nanostars and Rhodamine B samples might be a system error from the microscope.

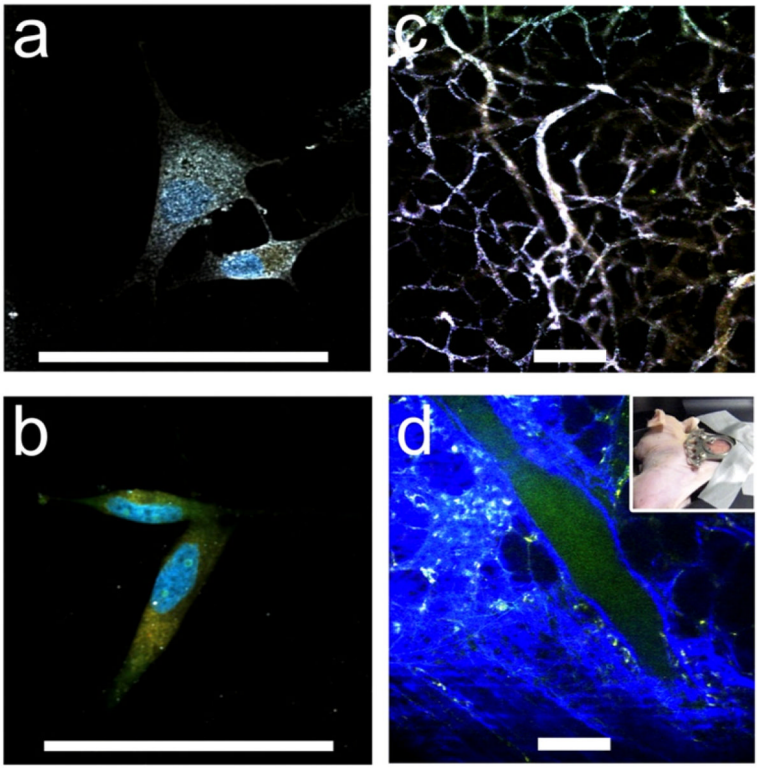

Figure 4.

((a), (b)) TPL imaging of nanostars S30, WGA-coated (a) versus PEGylated control (b), on BT549 cancer cells. WGA-nanostars labelled cells excited under 1% transmission at 800 nm showing preferential cell membrane binding. The blue and orange colours were from Hoescht 33342 and FM 1-43FX dyes respectively. The white colour of nanostars indicates a composite of similar intensities from three different detector channels. ((c), (d)) TPL imaging through a dorsal window chamber (inset) on a nude mouse. (c) With nanostars, tissue vasculature was visible under 5% transmission with minimal background fluorescence. (d) Without nanostars, it required 20% transmission to see vessels. The blue and green colours were from the collagen and blood. Scale bar: 100 μm.